Nanoscale

Accepted Manuscript

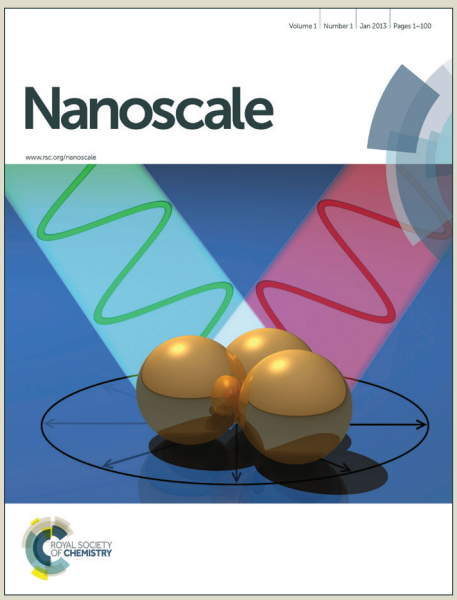

ROYAL SOCIETY OF CHEMISTRY

www.rsc.org/nanoscale

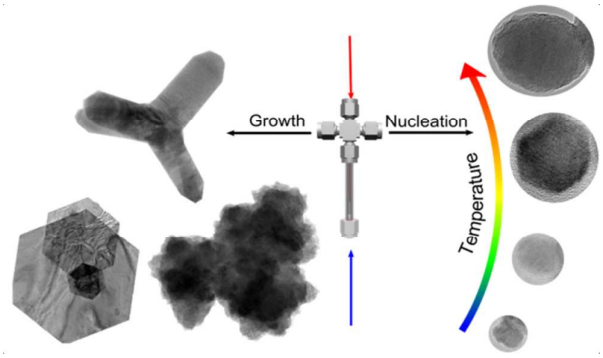

A continuous hydrothermal method has been applied to the synthesis of a wide range of metal sulphide nanomaterials with size and shape control.

Journal Name

RSCPublishing

ARTICLE

The Rapid Size- and Shape-Controlled Continuous Hydrothermal Synthesis of Metal Sulphide Nanomaterials

Cite this: DOI: 10.1039/x0xx00000x

Received 00th January 2012,
Accepted 00th January 2012

DOI: 10.1039/x0xx00000x

www.rsc.org/

Peter W. Dunne, Chris L. Starkey, Miquel Gimeno-Fabra and Edward H. Lester.

Continuous flow hydrothermal synthesis offers a cheap, green and highly scalable route for the preparation of inorganic nanomaterials which has predominantly been applied to metal oxide based materials. In this work we report the first continuous flow hydrothermal synthesis of metal sulphide nanomaterials. A wide range of binary metal sulphides, ZnS, CdS, PbS, CuS, $Fe_{(1-x)}S$ and Bi_2S_3, have been synthesised. By varying the reaction conditions two different mechanisms may be invoked; a growth dominated route which permits the formation of nanostructured sulphide materials, and a nucleation driven process which produces nanoparticles with temperature dependent size control. This offers a new and industrially viable route to a wide range of metal sulphide nanoparticles with facile size and shape control.

Introduction

Metal sulphides constitute a diverse and important class of materials. The wide range of structures, properties and applications exhibited by metal sulphides make them of interest both scientifically and industrially. Metal sulphide nanomaterials such as zinc, cadmium and lead sulphide are among the quintessential quantum dot materials.[1-3] A vast library of research is devoted to exploring their size and shape dependent optoelectronic properties for applications in biomedical imaging,[4] LEDs[5] and photovoltaic cells.[6] Covellite phase CuS was the first naturally occurring mineral found to exhibit superconductivity.[7] It is also investigated for its unusual optical properties,[8, 9] and potential use as a battery material.[9] Iron sulphides, which display a wide range of stoichiometries from Fe_3S_4, to FeS_2 with intermediary phases $Fe_{(1-x)}S$ and $Fe_{(1+x)}S$,[10] are commonly studied owing to their importance in biological systems, including iron reducing and magnetotactic bacteria.[11] They are also under investigation as environmental remediation agents for the removal of heavy metals[12] and as promising candidates for cathode materials in lithium ion batteries.[13] Other metal sulphides such as Bi_2S_3 are being considered as viable replacements for the toxic telluride-based thermoelectric materials.[14]

The synthesis of metal sulphide nanomaterials has previously been performed in myriad ways, including hot-injection,[15, 16] thermolysis of single source precursors,[17, 18] and hydro/solvothermal routes.[19-23] The hot-injection method is perhaps the classic technique for the synthesis of quantum dot materials. In this method a metal salt or, more commonly, a metal-organic complex is dissolved in a high boiling point solvent (oleylamine, dodecylamine, trioctylphosphine oxide, *etc*.) and heated. Injection of a sulphur source initiates nucleation and additional sulphur may then be introduced to promote further growth. Thermolysis routes also typically involve the use of high-boiling point solvents, in which single source precursors, generally metal thiol complexes, are dissolved. Heating these solutions to high temperatures causes the thermolysis of the precursor to yield the metal sulphide. Microfluidic syntheses have also been investigated for the synthesis of metal chalcogenide based quantum dots by de Mello[24] and Alivisatos.[25]

Hydrothermal techniques have also recently been explored for the synthesis of metal sulphide nanomaterials. These methods involve carrying out a reaction in a sealed vessel, allowing temperatures above the boiling point of water to be achieved. Hydrothermal processing has gained significant favour in recent years, particularly in the synthesis of oxide nanomaterials.[26-29] The increasing popularity of hydrothermal synthesis is thanks in large part to the high degree of control over the composition, size and shape of the obtained nanomaterials. Highly crystalline nanoparticles can also be obtained at lower temperatures than more traditional ceramic and sol-gel routes, which often require high temperature calcination and annealing steps. This, combined with the use of water as a reaction medium, rather than more exotic high boiling-point solvents, make the hydrothermal method significantly more environmentally benign than the conventional methods described above.

While hydrothermal strategies offer many advantages, they remain largely as batch processes. As such there exist inherent

difficulties in scale-up due to issues involving heat transfer, mixing and batch-to-batch reproducibility. Over the past twenty years continuous flow hydrothermal and solvothermal synthesis methods have been investigated as highly promising one-step processes for the production of inorganic nanomaterials,[30-36] with the potential to provide a wide variety of nanoparticles cheaply and effectively at the scales required to supply the increasing industrial demand for functional nanomaterials.

The continuous flow hydrothermal synthesis method, as pioneered by Adschiri *et al.*,[30, 37] exploits the tuneable properties of supercritical water to facilitate the fast nucleation of metal oxide nanoparticles. The increased pK_a and decreased dielectric constant of supercritical water when brought into contact with an unheated metal salt stream causes the formation and immediate nucleation of metal oxide nanoparticles, in many ways replicating the hot-injection method.[32] Since the initial reports of this technique a great deal of the research effort in this field has been focused on optimising the design of reactors[38-43] to improve the mixing dynamics and further facilitate the controlled nucleation of metal oxides to achieve small sizes and high degrees of monodispersity. It is only recently that continuous hydrothermal and solvothermal techniques have been applied to non-oxidic materials. A number of groups have reported the continuous flow hydrothermal synthesis of lithium iron phosphate.[44, 45] Hydroxyapatite has been synthesised continuously by Chaudhry *et al.*,[46] while our group have reported on the controlled continuous flow hydrothermal synthesis of hydroxyapatite nanorods and nanotubes.[47] The continuous solvothermal synthesis of metal nanoparticles has been reported by Choi *et al.*[48] and an aqueous route was developed by Aksomaityte *et al.*[49]. Continuous solvothermal synthesis has also recently been used to produce metal organic frameworks.[50]

We aim to further expand the scope of the continuous hydrothermal method by applying it to the synthesis of classes of materials previously unexplored by this technique. This work represents the first use of continuous flow hydrothermal processing for the synthesis of a wide range of metal sulphide nanomaterials, with size and shape control over the obtained particles achieved by simple modifications to the reaction conditions.

Materials and Methods

Materials

All materials were purchased from Sigma-Aldrich and used as received. $Zn(NO_3)_2.6H_2O$, $Cd(NO_3)_2.4H_2O$, $Pb(NO_3)_2$, $Cu(NO_3)_2.2.5H_2O$, $FeSO_4.7H_2O$, and $Bi(NO_3)_3$ were used as the metal sources. All salts were dissolved in the appropriate amounts of de-ionised water prior to use, with the exception of $Bi(NO_3)_3$, which was dissolved in a 5% nitric acid solution to prevent the formation of the insoluble sub-nitrates. In all cases thiourea was used as the sulphur source.

Reactor

All reactions were carried out using the vertically aligned counter-current mixing reactor designed by Lester *et al.*,[39] shown in Figure 1., which has been described in detail elsewhere.[51] Briefly the continuous flow reactor, constructed using Swagelok® high pressure fittings, comprises of an outer tube of 3/8" diameter, with a wall thickness of 0.065", and an inner 1/8" diameter tube with a wall thickness of 0.035", both 316 stainless steel. Gilson HPLC piston pumps deliver water to a preheater and downwards through the inner pipe, while the metal salt solution is pumped upwards through the outer pipe. Mixing of the heated downflow and cool upflow induces crystallisation of the products, which are then passed through heat exchangers before being discharged from the system. Pressure is maintained at ~250 bar by a manual back-pressure regulator.

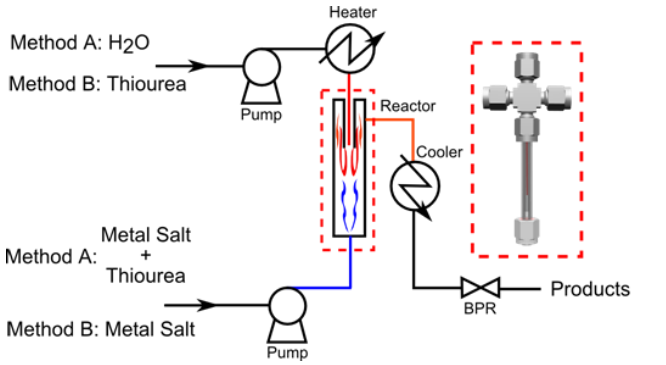

Figure 1. A simplified schematic of the counter-current continuous flow reactor used in this work.

Two methods have been developed for the continuous synthesis of metal sulphide nanomaterials:

Method A

A solution of metal salt is prepared, typically at 0.05 M. To this is added sufficient thiourea to provide a two-fold excess of sulphur relative to the stoichiometry of the expected product. This mixed metal/thiourea solution is fed upwards as the unheated stream and brought into contact with the heated water stream. Using this method it has been found that temperatures of ~400 °C are required to break down enough thiourea to create the active sulphur source needed to produce significant yields within the short contact time.

Method B

Metal salt solutions, typically 0.025 M in de-ionised water, are pumped as the unheated up-flow, while a separate solution of thiourea is pumped through the preheater as the downflow. Passing the thiourea through the preheater provides a longer residence time for the decomposition to occur, and thus the temperature of the heater may be varied between 250 °C and 400 °C.

Unless otherwise stated the flow rates in both methods were maintained at 20 mL min^{-1} for the downflow and 10 mL min^{-1} for the upflow. Products were obtained as aqueous suspensions. Powders were isolated and washed with de-ionised water by repeated centrifugation steps before drying overnight at 70 °C. Further synthesis details are provided in the ESI.

Characterisation

Powder X-ray diffraction patterns were typically recorded using a Bruker D8-Advance diffractometer with Cu K_α radiation (λ = 1.5418 Å). A 2 θ range of 5 to 70° was scanned with a step size of 0.04° 2θ and a collection time of 6 s/step. Crystallite diameters were calculated using the Scherrer equation from line broadening determined with the program Xfit.[52] Selected patterns were subject to full Rietveld refinement performed using the GSAS suite implemented through EXPGUI.[53, 54] Transmission electron micrographs were obtained using a JEOL 2100F at an accelerating voltage of 200 kV. Samples were prepared for transmission electron microscopy by resuspending the dried powders in acetone with sonication and deposited on 300 mesh lacey carbon coated copper grids.

Results

ZnS

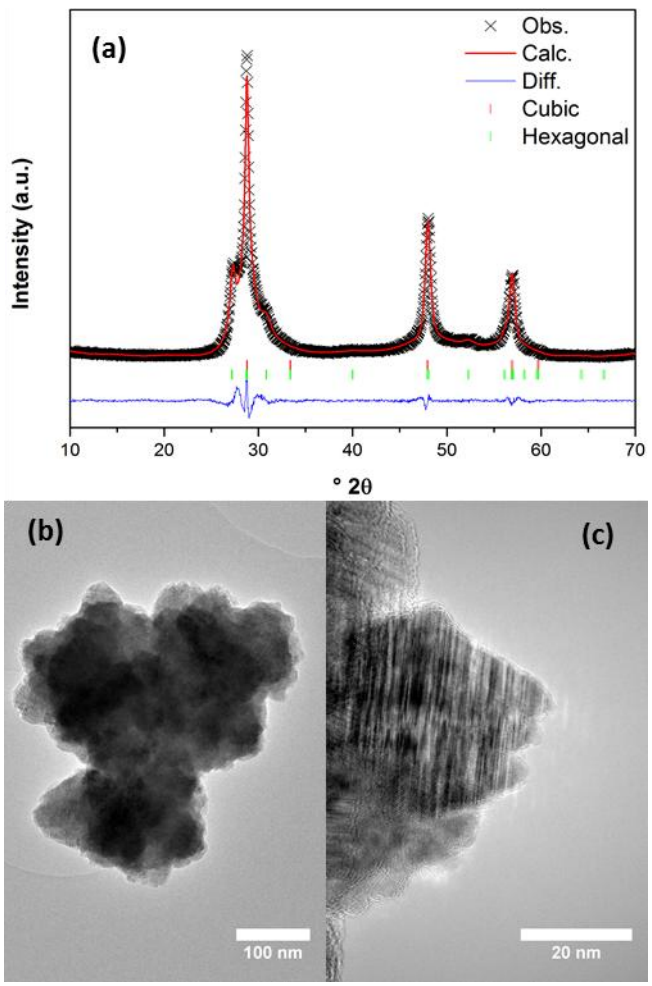

Figure 2. The refined XRD pattern (a) and TEM images of ZnS prepared by Method A. Reitveld refinement was performed with both cubic ($F\bar{4}3m$, a = 5.3656 Å) and hexagonal ($P6_3mc$, a = 3.7846 Å, c = 6.2089 Å) phases.

The XRD pattern of ZnS obtained by Method A is shown in Figure 2a. Rietveld refinement shows that the product is comprised of a mixture of 58% cubic sphalerite and 42% hexagonal wurtzite phase ZnS, with average crystallite diameters of 12.4 and 22.6 nm respectively. TEM images (Figure 2b & c) show large agglomerates with diameters of ~200 nm. High magnification imaging reveals these agglomerates to be comprised of smaller nanocrystalline domains, as expected based on the refinement results. In addition streaking/striations are visible, indicative of a significant amount of twinning or stacking faults. This is a commonly observed phenomenon with zinc sulphide materials,[55-57] due to the closely related cubic and hexagonal phases. Furthermore, the flower-like shape of the agglomerates is likely to result from this twinning. Similar morphologies have often been observed in sphalerite-wurtzite systems,[58-62] with the growth of hexagonal phase petals from a cubic phase core being a common occurrence in mixed cubic/hexagonal phase systems.

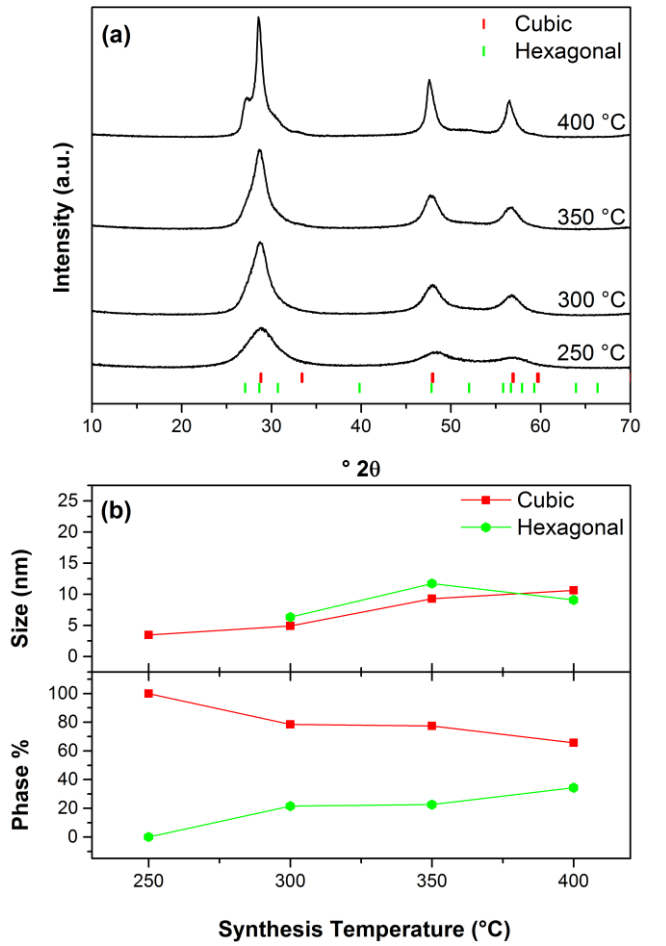

Figure 3. The XRD patterns (a) and calculated crystallite diameters and phase percentages from Reitveld refinements (b) of the ZnS nanoparticles obtained by Method B.

The XRD patterns of the ZnS obtained by Method B are shown in Figure 3a. From the XRD patterns it is apparent that increasing the temperature from 250 °C to 400 °C leads to both a general increase in crystallite size and a transformation from pure sphalerite to a mixture of the sphalerite and wurtzite phases at higher temperatures.

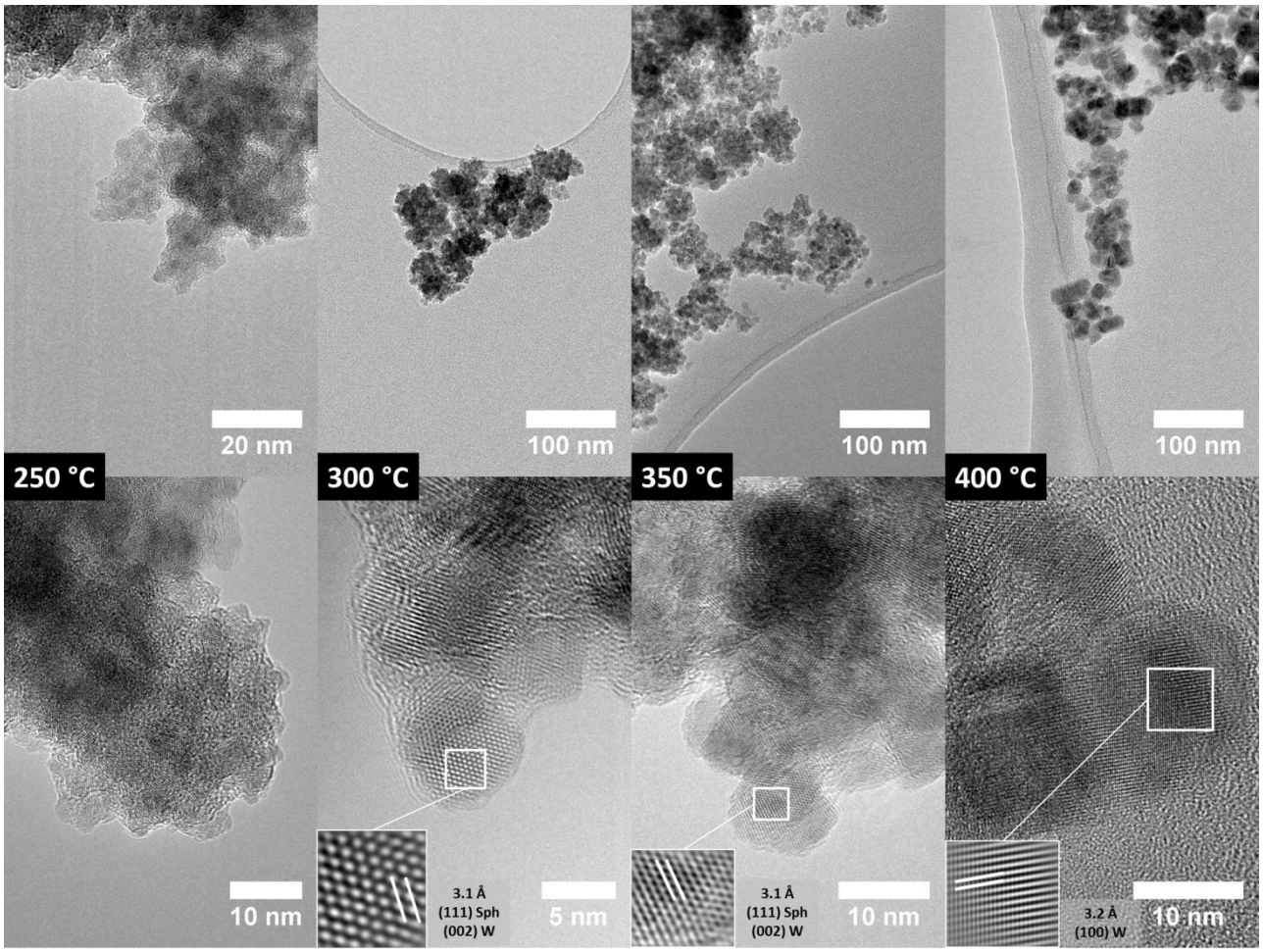

Figure 4. TEM images of ZnS nanoparticles obtained by Method B at the indicated synthesis temperatures. Insets show reconstructed images highlighting crystal planes of the cubic sphalerite (Sph) and hexagonal wurtzite (W) phases of ZnS.

The hexagonal wurtzite phase content increases from 0% at a synthesis temperature of 250 °C to ~22% at temperatures of 300 °C and 350 °C, while the sample prepared at 400 °C contains 34% wurtzite. The calculated crystallite diameters of the cubic sphalerite phase increases with increasing synthesis temperature, from 3.5 nm at 250 °C, to 4.9 nm at 350 °C. The samples prepared at 350 °C and 400 °C both have crystallite diameters close to 10 nm. The calculated diameters of the hexagonal wurtzite phase increases from 6.3 nm to 11.7 nm on increasing the reaction temperature from 300 °C to 350 °C, followed by a decrease in size to 9 nm on further increasing the synthesis temperature to 400 °C, possibly due to increased supersaturation under supercritical conditions. Table 1 and Figure 3b show the phase composition and crystallite diameters of the four ZnS samples prepared by Method B as calculated from the Reitveld refinements shown in Figure S1 (ESI).

TEM images of the ZnS obtained by Method B, Figure 4, show that the products obtained at temperatures up to 350 °C are comprised of agglomerated nanocrystals. The crystalline domain sizes are consistent with those obtained from analysis of the XRD data. Synthesis at 400 °C affords larger less agglomerated cuboidal crystallites, again with sizes matching those predicted by XRD analysis. The fluorescence spectra of all ZnS samples are shown Figure S3 (ESI).

Table 1. Phase composition and calculated crystallite diameters, D, of cubic sphalerite (Sph) and hexagonal wurtzite (W) phases of ZnS samples prepared by Method B.

T/°C	$\%_{Sph}$	$\%_{W}$	D_{Sph}/nm	D_{W}/nm
250	100	0	3.5	-
300	78.4	21.6	4.9	6.4
350	77.4	22.6	9.3	11.8
400	65.6	34.4	10.6	9.1

The good agreement between the sizes of the crystallites observed by TEM and calculated by XRD suggests that the two phases exist as separate crystallites, rather than as twinned crystals (this is further evidenced by the apparent single crystalline nature of the particles observed by HRTEM).

The large size of the agglomerated particles and the significant twinning observed in the material prepared by Method A, wherein both the zinc nitrate and thiourea are fed against a superheated water stream, suggests a growth dominated mechanism, whereby the decomposition of thiourea to an active

sulphur source such as HS^- happens concurrently with the formation of the zinc sulphide, leading to a slow growth dominated process which allows for the intergrowth of the two phases. In contrast, Method B, where the thiourea is first broken down by being fed separately through the preheater, promotes a nucleation driven process due to the immediate availability of HS^- forcing the rapid nucleation and precipitation of very small ZnS nanoparticles.

It has previously been suggested that the formation of ZnS nanoparticles proceeds via the aggregation of molecular clusters with the nature of the clusters determining the phase of the product formed.[63] Smaller $Zn_3S_3(H_2O)_6$ and $Zn_4S_6(H_2O)_4^{4-}$ clusters which favour sphalerite formation are formed at lower S/Zn ratios, while the larger $Zn_6S_6(H_2O)_9$ clusters formed at higher ratios promote wurtzite formation. At the lowest synthesis temperature of 250 °C the breakdown of thiourea to HS^- is incomplete, leading to a lower S/Zn ratio. As such the formation of the kinetically favoured sphalerite phase is promoted at this synthesis temperature. Elevation of the reaction temperature leads to a more complete breakdown of the thiourea increasing the S/Zn ratio, which, combined with the enhanced stability of the wurtzite phase at higher temperatures due to entropy effects permits the nucleation of the wurtzite phase.

CdS

The synthesis of cadmium sulphide by Method A results in a mixture of 11% cubic hawleyite and 89% hexagonal greenockite phase CdS, as shown by the XRD pattern in Figure 5a. The TEM images of this product, Figure 5b & c, reveal a mixture of rod and multipodal morphologies. Several clearly defined tetrapodal nanoparticles are also observed with 40 nm diameter cores and 100 nm long arms. These morphologies are well-established in regards to cadmium sulphide and selenide nanomaterials,[64-66] and arise from the same cubic/hexagonal intergrowth phenomenon discussed in relation to the sphalerite-wurtzite system. The cubic and hexagonal phases of CdS are closely related, with the c-face of the hexagonal phase being related to the (111) plane of the cubic phase by a simple rotation operation. It has been shown, both computationally and experimentally through *in-situ* transmission electron microscopy, that spherical cadmium selenide nanoparticles undergo a thermally induced surface rearrangement to the hexagonal phase. The transformation gives a similar (if stunted) tetrapodal morphology[67] to that seen here. It may be suggested that this product is formed by the initial nucleation of the kinetically favored cubic phased nanoparticles, which at the elevated temperatures employed here undergo a surface rearrangement to give hexagonal phase capping on the (111) faces of the cubic core. This may result in a tetrahedral or multifaceted arrangement. Further deposition of material then causes growth of the hexagonal phase arms leading to the morphologies observed here.[68] The rod-like structures likely arise from the direct growth of nucleated hexagonal phase nanoparticles.

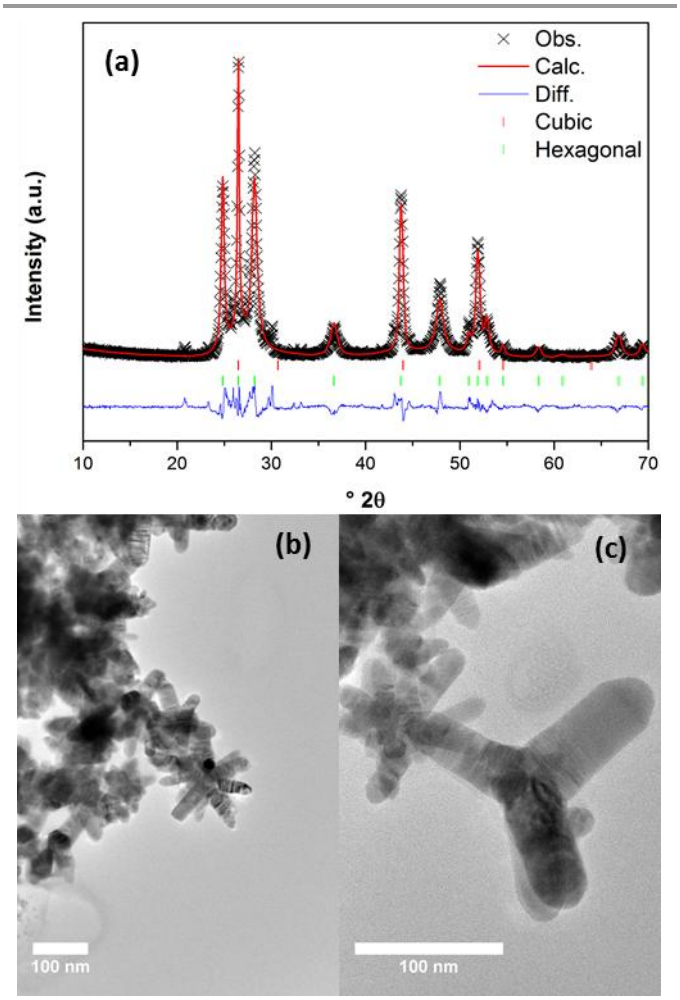

Figure 5. The refined XRD pattern (a) and TEM images of CdS prepared by Method A. Reitveld refinement was performed with both cubic ($F\bar{4}3m$, a = 5.8365 Å) and hexagonal ($P6_3mc$, a = 4.1361 Å, c = 6.7222 Å) phases.

As with zinc sulphide, the synthesis of cadmium sulphide by Method B results in the formation of very small nanoparticles. The XRD patterns, refined compositions and crystallite diameters are shown in Figure 6 and Table 2 (see Figure S2 for refinement results). At synthesis temperatures of 250 °C the sample consists of 72% cubic hawleyite and 28% hexagonal greenockite phases. The hexagonal phase content increases to 35% at 300 °C, while those samples prepared at 350 °C and 400 °C are comprised of a close to 50:50 mix of the two phases. The calculated crystallite diameters of both phases are ~7.3 nm and ~8.5 nm when prepared at 250 °C and 300 °C, respectively. Increasing the temperature to 350 °C increases the size of the cubic and hexagonal phase crystallites to 13.6 nm and 16.3 nm. Similar sizes are obtained for the 400 °C sample.

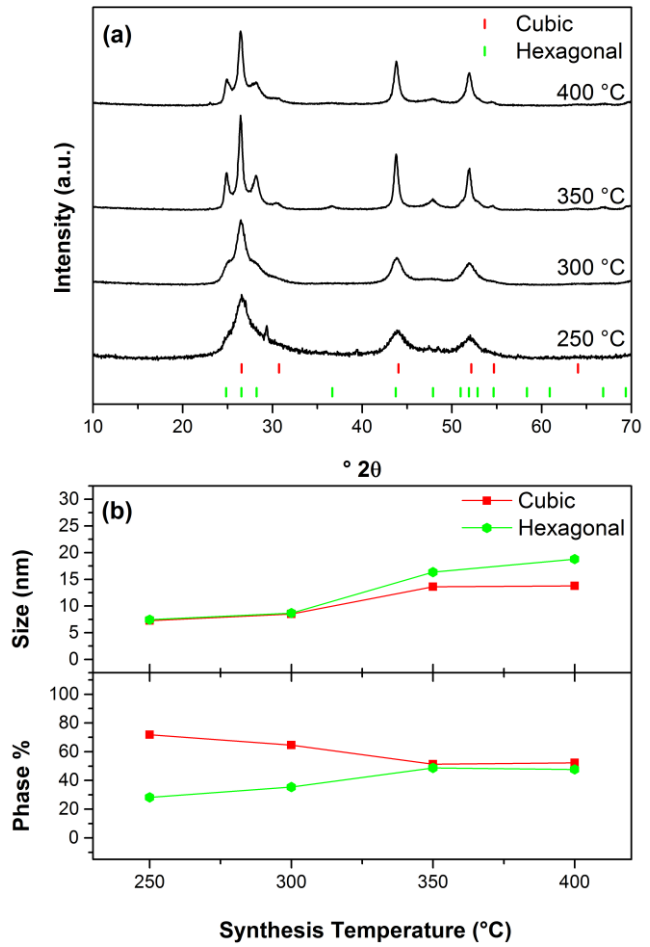

Figure 6. The XRD patterns (a), crystallite diameters and phase percentages calculated from Reitveld refinements (b) of the CdS nanoparticles obtained by Method B.

The TEM images of the obtained products, Figure 7, show that, aside from the sample prepared at 250 °C, the cadmium sulphide is generally less agglomerated than the zinc sulphide produced by the same method. The crystallite sizes of the nanoparticles observed by TEM are in good agreement with those calculated from the XRD patterns. HRTEM images of the products obtained at reaction temperatures of 250 °C and 300 °C show that the nanocrystals, with calculated sizes of less than 10 nm, exhibit some stacking faults and twinning. The extremely small sizes and consequent high surface energies of these nanoparticles may promote the thermal transformation to the more stable hexagonal phase CdS. In the case of the 250 °C sample this may be further exacerbated by the high degree of agglomeration which would give a greater number of particle-particle interfaces at which stacking faults may develop. Interestingly a number of the roughly spherical particles in the 300 °C sample were seen to have undergone a surface rearrangement to yield stunted tetrapodal morphologies. This further confirms the proposed mechanism of formation of the tetrapods synthesised by Method A. The products obtained at 350 °C which showed a 50:50 mixture of the cubic and hexagonal phases and larger sizes was found to be comprised largely of unagglomerated single phase nanocrystals. This may indicate that the increase in size brought about by the higher synthesis temperatures is sufficient to stabilise the cubic phase against the thermal transformation to the hexagonal phase, such that each phase nucleates and crystallises separately, as was the case with the ZnS samples. The sample prepared at 400 °C consists of larger, somewhat elongated particles. Individual crystallites are observed with sizes in good agreement with calculated crystallite diameters; however many of the particles appear to be the result of the fusion of individual crystallites with twinning and stacking faults at the interfaces. The generation of these stacking faults is consistent with particle growth through oriented attachment processes, wherein the hexagonal phase may propagate throughout the conjoined crystal from the point of contact.[69]

Table 2. Phase composition and calculated crystallite diameters, D, of cubic hawleyite (H) and hexagonal greenockite (G) phases of CdS samples prepared by Method B.

T/°C	$\%_H$	$\%_G$	D_H/nm	D_G/nm
250	71.7	28.3	7.2	7.4
300	64.6	35.4	8.5	8.7
350	51.2	48.8	13.6	16.3
400	52.3	47.7	13.8	18.8

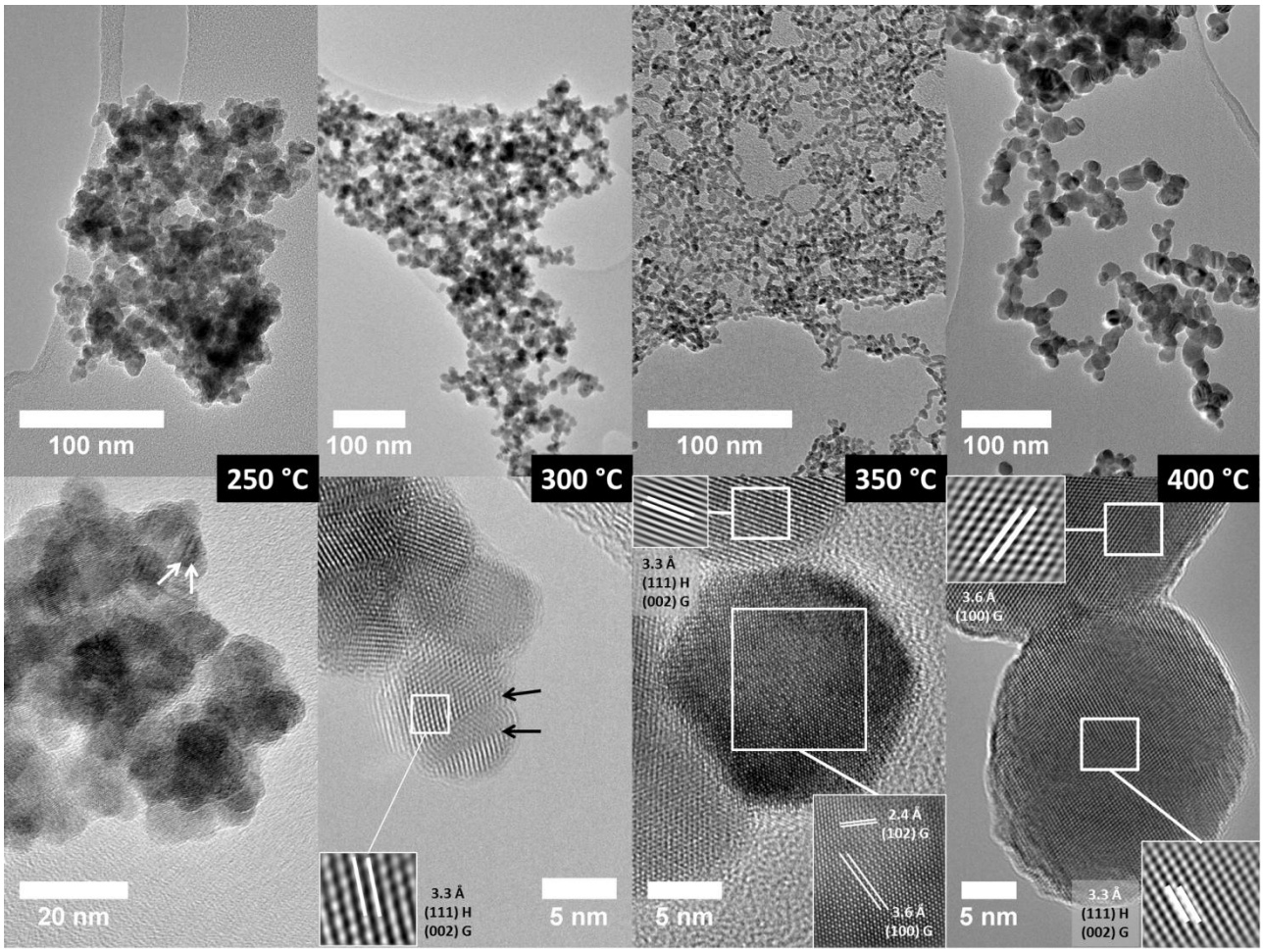

Figure 7. TEM images of CdS nanoparticles obtained by Method B at the indicated synthesis temperatures. Insets show reconstructed images highlighting crystal planes of the cubic hawyleyite (H) and hexagonal greenockite (G) phases of CdS.

PbS

Attempts to synthesise lead sulphide by Method A formed a mixture of lead sulphide and lead sulphate (Figure S4). We attribute this to the presence of nitrate in conjunction with the high temperatures required to break down the thiourea in the short contact time (< 5s). The resulting highly oxidising environment causes the formation of lead sulphate. This a common problem in the synthesis of lead sulphide nanomaterials.[70] Despite this issue the poor solubility of most other lead salts (and the difficulty this poses for pumping solutions through the reactor) means that lead nitrate remains the most suitable precursor for lead sulphide synthesis. Method B, wherein the thiourea is decomposed in the preheated stream prior to contact with the metal source permits the use of significantly lower reaction temperatures, which limit the oxidising potential of the system. This allows the formation of lead sulphide without lead sulphate contamination.

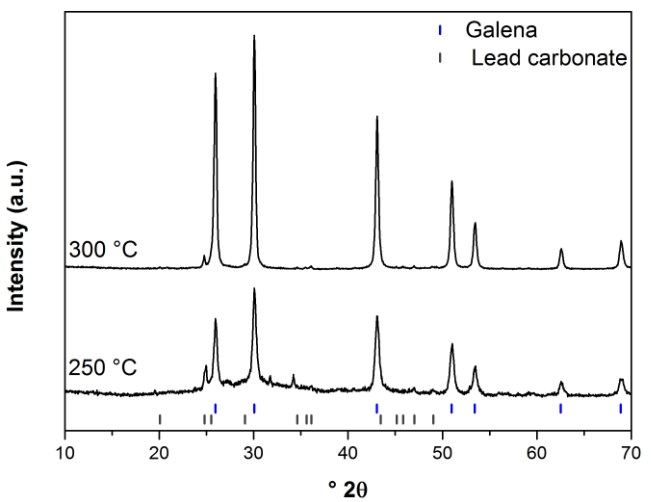

Figure 8. XRD patterns of PbS samples prepared by Method B at 250 °C and 300 °C. The main product is galena with only minor lead carbonate impurities.

The XRD patterns of the lead sulphide nanoparticles obtained by Method B at reaction temperatures of 250 °C and 300 °C are shown in Figure 8. In both cases lead carbonate is present as a

minor impurity phase, however lead sulphate is not observed. The major product of both reactions is galena, cubic lead sulphide. Lead sulphide, unlike zinc and cadmium sulphide, does not possess any other polymorphs. Scherrer analysis was sufficient to estimate the crystallite diameters as 15 nm and 27 nm for particles synthesised at 250 °C and 300 °C, respectively.

The TEM images of both products, Figure 9, confirm the crystallite sizes calculated by Scherrer analysis. The obtained lead sulphide nanoparticles are highly crystalline, and generally presented as cuboidal in shape, though a small number of octahedral particles were also observed. Complex hyper-branched lead sulphide nanostructures are common in the literature.[71-73] These are invariably the result of prolonged or slow reactions, which would promote growth. The extremely small cuboidal nanoparticles obtained here are thus consistent with a nucleation dominated process, with temperature dependent size control, as observed for both ZnS and CdS.

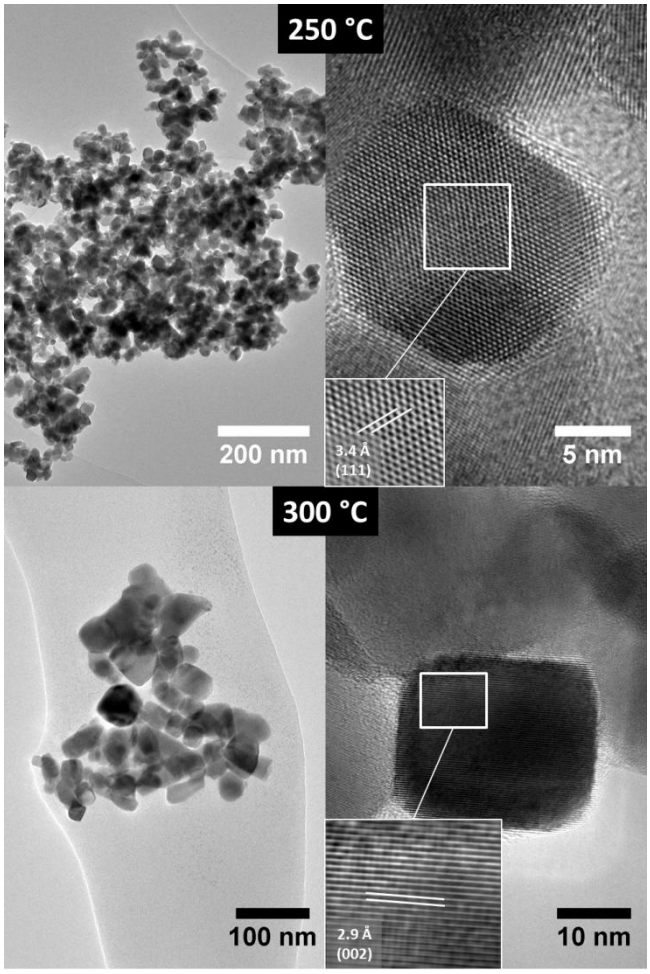

Figure 9. TEM images of cuboidal PbS nanoparticles obtained by Method B at 250 °C and 300 °C. Insets show reconstructed images highlighting crystal planes of the cubic galena PbS.

CuS

The synthesis of copper sulphide also proved difficult at the higher temperatures required by Method A. The product obtained is a mixture of digenite and poorly crystalline covellite. It is likely that covellite is formed initially; however covellite has very low melting and decomposition temperatures. It was found that the material produced aggregates inside the pipework, which hampers collection efficiencies (see ESI, Figure S5, for the XRD pattern and TEM images of this product).

On attempting to synthesise CuS at 250 °C using Method B it was found that a white powder was obtained, identified as copper(I) thiocyanate, CuSCN (Figure S6). Thiocyanate complexes were not observed in any other case. It is quite likely that at lower temperatures the thiourea undergoes a rearrangement to the tautomeric ammonium thiocyanate,[74] while only a portion decomposes to HS^-. It was observed in all systems that the reaction at 250 °C generally gave lower yields, which may be a result of this incomplete breakdown to HS^-. With all other metals studied the presence of thiocyanate is unlikely to interfere significantly with the formation of the sulphides, as many of the metal thiocyanate complexes are soluble, and thus the metal will remain available to react with HS^- to give the sulphide, or would remain in solution and be removed on washing. In the case of Cu(II), the formation of $Cu(SCN)_2$ is immediately followed at elevated temperatures by disproportionation to the insoluble Cu(I) complex CuSCN (and indeed this is a common technique for the gravimetric determination of copper).[75] Cuprous thiocyanate will thus be the major product obtained at temperatures sufficient to promote the thiourea/ammonium thiocyanate isomerisation but not enough to completely decompose the thiourea.

As a result of the low melting point of covellite and the formation of CuSCN at lower reaction temperatures, there exists a narrow window in which pure, crystalline covellite phase CuS may be obtained. In order to achieve this the synthesis was carried out by Method B, with the preheater temperature at 300 °C to ensure full decomposition of the thiourea to HS^-, while also maintaining low post-mixing temperatures to avoid melting or decomposing the covellite. Using this approach pure, nanocrystalline covellite phase CuS was obtained, and the XRD pattern and TEM images of the product are shown in Figure 10.

While the precise nature of the bonding in covellite remains a source of some contention[76] the structure may generally be described as consisting of a layer of trigonal CuS_3, giving a graphitic structure parallel to the (001) plane, with tetrahedral CuS_4 units above and below this layer. The S atoms of the graphitic layer form the vertices of two tetrahedral CuS_4 above and below the plane resulting in very strong bonding within this "tetrahedron bilayer". Bonding between these bilayers through disulphide linkages in the c-direction is significantly weaker.[77] Given the highly anistropic nature of the covellite structure hexagonal platelet formation is expected, and indeed is quite common, with many copper sulphide nanostructures consisting of self-assembled hexagonal plates.[78-80]

Analysis of the XRD pattern of the covellite material obtained here reveals the product to be entirely pure; however it was noted that the peak intensities did not match those of the standard covellite patterns. The inset in Figure 10a shows the fitted peak areas of the sample normalised relative to the calculated peak areas of a standard pattern simulated from the covellite structure (*P6₃/mmc*, a = 3.7909, c = 16.3764). This reveals that reflections from the (110) plane are highly overrepresented. This indicates a much higher degree of crystallinity in the (110) direction, suggesting a plate-like morphology, as would be expected given the crystal structure. Scherrer analysis gives crystallite diameters of 39.2 nm and 38.3 nm in the (100) and (110) directions, respectively, while the four observed (00l) reflections give an average thickness in the c-direction of 24.4 nm. The smaller size in this direction suggests the formation of planar covellite nanocrystals.

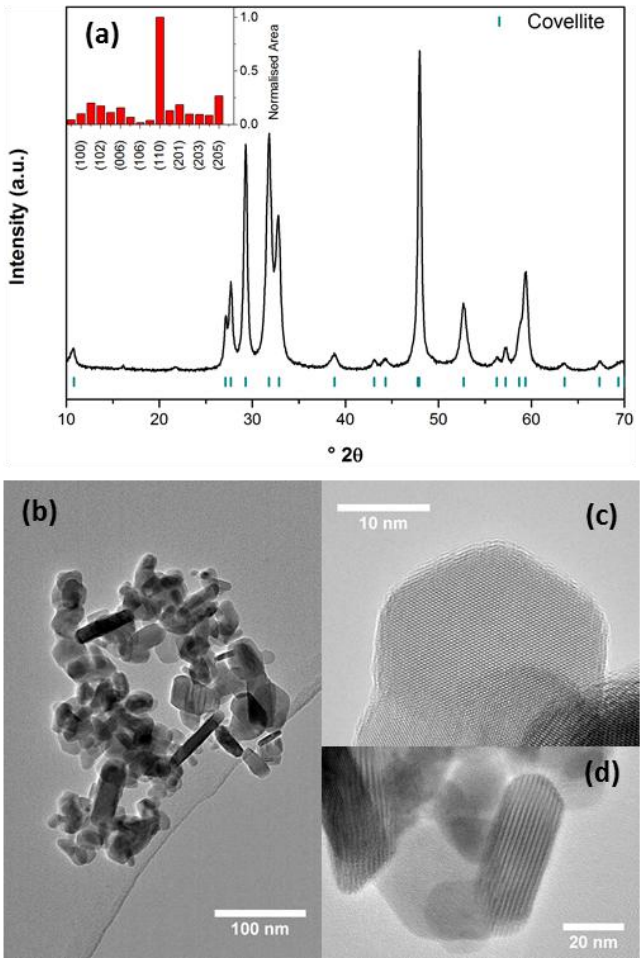

Figure 10. The XRD pattern of the CuS obtained by Method B at 300 °C (a), tick marks indicate the major reflections of covellite, and TEM images showing the hexagonal platelet morphology (b-d).

The TEM images show that the sample is comprised mainly of hexagonal nanoplates, in agreement with the X-ray diffraction results. A number of extremely thin hexagonal sheets were observed, which may potentially be single sheets of the bilayers described above, while the majority of the nanoplates are comprised of stacked layers of these nanosheets (Figure S7). Even under nucleation conditions the highly anisotropic structure of covellite would result in the formation of hexagonal nanostructures. As such it may be suggested that the nucleation mechanism inferred for the previous syntheses carried out by Method B is still in effect in the synthesis of CuS.

$Fe_{(1-x)}S$

The synthesis of iron sulphide materials was attempted using both Method A and Method B. All products were initially black, however the materials prepared by Method B at temperatures below 400 °C were seen to develop an orange coloration almost immediately, caused by the formation of lepidocrocite, γ-FeOOH (Figure S8, ESI). It is reasonable to suggest that the lepidocrocite is generated as a result of the inherent instability of pyrrhotite,[81] compounded by the small particle sizes expected of this synthesis approach. Samples prepared at the higher temperature of 400 °C by both Method A and B were found to be stable, and the XRD patterns of these stable products are shown in Figure 11.

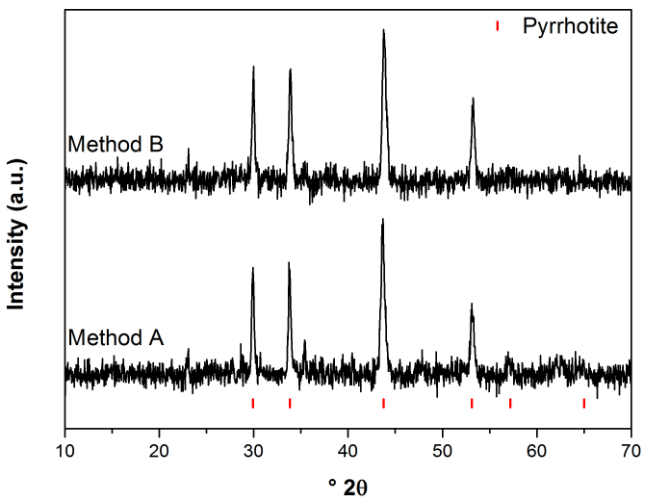

Figure 11. XRD patterns of the stable iron sulphide products obtained by synthesis at 400 °C by Method A and Method B.

The collected patterns are consistent with the pyrhhotite phase, $Fe_{1-x}S$ (x = 0 – 0.125) with the hexagonal NiAs structure. Unfortunately, due to the fluorescence of iron under Cu K_α irradiation, more detailed analysis was not feasible. TEM images of both pyrrhotite products are shown in Figure 12. The sample prepared by Method A show very large, thin hexagonal plates with widths ranging between 0.5 and 1 micron and a typical thickness of only 30 nm. In contrast, Method B leads to the formation of significantly smaller particles. These also possess a hexagonal morphology; however they are far less anisotropic, and more monodisperse in size with the majority of particles having a width of ~100 nm and a thickness of 30 nm. These results are consistent with those of Lai and Chen,[82] who have shown that pyrrhotite forms large hexagonal plates through the oriented attachment of smaller hexagonal nuclei.

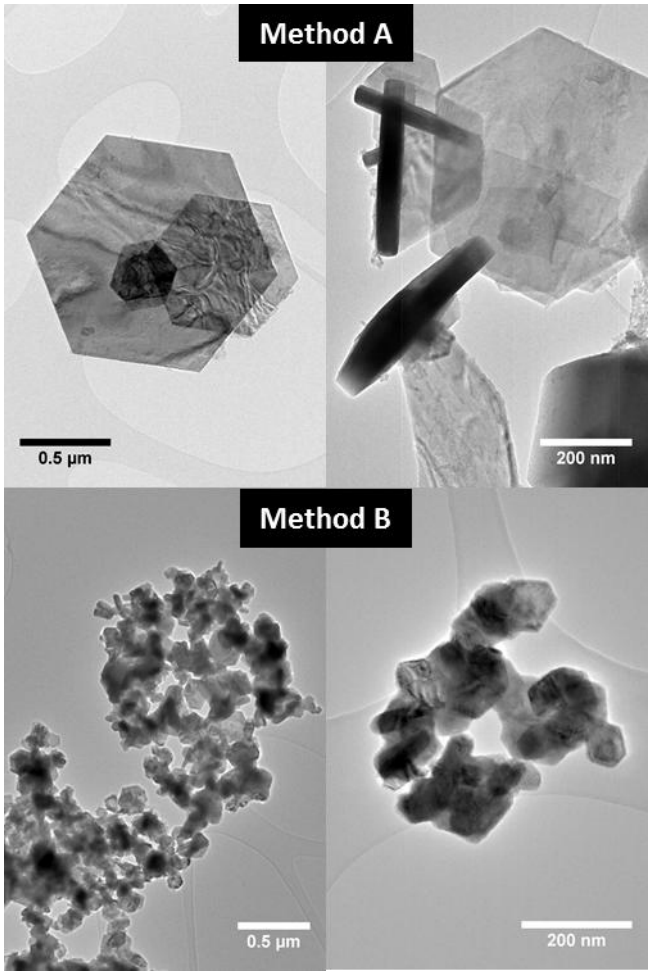

Figure 12. TEM images of pyrrhotite nanoplates and nanoparticles obtained by Method A and Method B at 400 °C.

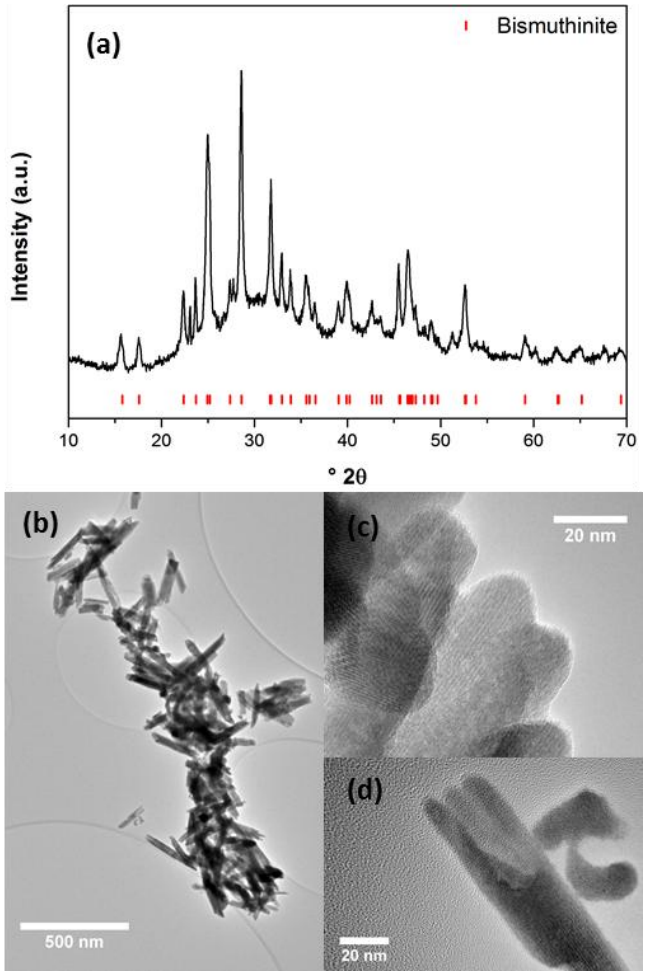

Figure 13. The XRD pattern (a), and TEM images (b - d), of the Bi_2S_3 self-assembled nanorods obtained by Method B with modified flow-rates.

Bi_2S_3

The poor solubility of bismuth nitrate necessitated the use of dilute nitric acid to obtain stable solutions suitable for pumping. It was found that all attempts at synthesising Bi_2S_3 with the same conditions used for other materials invariably formed $Bi_2O_2SO_4$. This is due to the highly oxidising environment created by the large excess of nitric acid and the high temperatures within the reactor. Based on previous results a minimum temperature of 400 °C is required to break down thiourea by Method A. It was found, however, that even using the typical Method B conditions at 250 °C that $Bi_2O_2SO_4$ was the main product. To mitigate the oxidising potential of the system it was necessary to alter the reaction parameters to maintain low post-mixing temperatures. This was achieved by varying the flow-rates of the system. The thiourea was flowed at a rate of 5 mL min^{-1} through the preheater, while the metal upflow was pumped at 10 mL min^{-1} (the concentrations were adjusted accordingly to maintain a two-fold excess of thiourea). These flow-rates facilitated the complete breakdown of thiourea to HS^-, while the greater flow of the unheated metal salt dilutes the heat further.

These modified conditions allowed pure Bi_2S_3 to be obtained. Figure 13 shows the XRD pattern and TEM images of the material produced under these modified conditions. The XRD pattern matches that of the expected product, bismuthinite, Bi_2S_3. Profile fitting using Xfit gave a calculated crystallite diameter of 19.5 nm. High resolution transmission electron microscopy reveals that the product adopts a rod-like morphology, a common morphology observed in bismuthinite nanomaterials.[21, 83-85] The nano-rods, with diameters of ~20 nm, are seen to self-assemble into larger razor-shell type nanostructures, a number of which appear to have fully closed, to give nanotubular arrangements. These morphologies are indicative of a combined nucleation, growth and oriented attachment mechanism. This contrasts significantly with the results of previous syntheses by Method B. This discrepancy can be explained by the lower temperatures and flow rates required for bismuth sulphide formation, which lead to longer residence times. The increased residence times promote the growth and self-assembly of these nanostructures from the nanoparticles which may be obtained from the initial nucleation step.

Discussion

The formation of the metal sulphide nanoparticles by both methods employed here is dependent upon the generation of hydrogen sulphide. The hydrothermal decomposition of thiourea serves as a convenient method to generate the required HS^-. By Method A, wherein thiourea is mixed with the metal salt and maintained at room temperature prior to mixing with the preheated water stream, very high temperatures in excess of 400 °C are needed to break down the thiourea within the extremely short contact time. By Method B, in which the thiourea is fed through the preheater, and thus is sustained at temperature for longer, temperatures as low as 250 °C are sufficient to generate significant amounts of HS^-. At this lowest temperature flow-rates of 10 mL min^{-1} result in residence times such that the decomposition is not entirely complete. At least some thiourea remains as the tautomeric form, ammonium thiocyanate, as evidenced by the formation of copper thiocyanate, and the generally low yields of other metal sulphide materials under these conditions. This may be overcome by lowering the flow-rate to confer longer residence times as was required for the formation of bismuth sulphide, or by increasing the temperature.

$$H_2NCSNH_2 \xrightarrow{T \leq 250\,^{\circ}C} NH_4SCN \quad (1)$$

$$H_2NCSNH_2 + H_2O \xrightarrow{T \geq 250\,^{\circ}C} NH_4OH + HCO_3^- + HS^- \quad (2)$$

$$M^{x+} + HS^- \xrightarrow{T \geq T_{form.}} MS_{x/2} \quad (3)$$

On bringing a mixed solution of thiourea and metal salt into contact with the superheated water stream, as per Method A, thiourea decomposition would occur almost immediately, increasing the hydrogen sulphide concentration; however this is offset by the concurrent precipitation of the metal sulphide, *i.e.*, reactions (2) and (3) occur at effectively the same time. This maintains the concentration of metal sulphide precursor at relatively low levels, and subsequently the rate of formation of the sulphide would be relatively low (though the reaction is still complete with residence times of ~1 second). This results in a growth dominated mechanism and the formation of metal sulphide nanostructures directed by the underlying crystal structure of the sulphide.

Method B physically and temporally separates the generation of HS^- and metal sulphide precipitation. Thiourea breakdown occurs within the preheater, prior to contact with the metal salt. The concentration of hydrogen sulphide at the mixing point is thus maximised, and the excellent mixing dynamics within the counter-current reactor used in this work cause immediate and intimate mixing with the metal stream rapidly increasing the metal sulphide precursor concentration. This drives the nucleation of the metal sulphide, forming nanoparticles. The formed nanoparticles exhibit temperature dependent sizes as may be expected based on classical nucleation theory.[86]

Figure 14 represents a simple schematic of the proposed mechanisms of both methods, based on the LaMer model,[87] where in this case the x-axis may be considered either as time or position within the reactor. C* signifies the critical nucleation threshold – the precursor concentration, or degree of supersaturation above which nucleation occurs. When the precursor concentration is below this point particles grow by diffusion, or, at high polydispersion, Ostwald ripening. Method A results in a post-mixing increase in precursor concentration (*i.e.* $[M^{x+}] + [HS^-]$) to a level above the nucleation threshold, but because of the competition between reactions (2) and (3), the concentration will lie below the critical point, within the growth domain. To obtain small monodisperse nanoparticles a rapid increase in precursor concentration above the nucleation threshold is required. The resultant supersaturation is relieved by the rapid nucleation of a large number of nanoparticles. It is clear that Method B satisfies these requirements, and consequently the products of this route are obtained as generally uniform and monodisperse ultrafine particles.

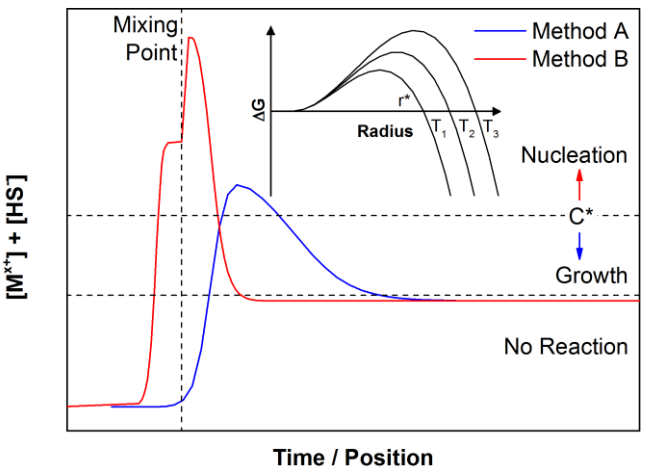

Figure 14. A simplified representation of the suggested mechanism of Method A and Method B based on the LaMer model.[87] The inset shows the influence of increasing temperature on critical nucleus radius.[86]

Conclusions

We have demonstrated for the first time the application of continuous hydrothermal methods to the synthesis of a wide range of binary metal sulphide nanomaterials. Thiourea has been employed as a sulphur source for the production of ZnS, CdS, PbS, CuS, $Fe_{(1-x)}S$ and Bi_2S_3 nanomaterials. Two different methods have been developed using a vertical reactor with counter-current mixing which ensures immediate and uniform mixing of reagent streams. By varying the point of addition of the thiourea different mechanisms may be invoked. On bringing a mixed stream of thiourea and metal salt into contact with a super-heated water stream a growth mechanism is promoted by the concurrent generation of HS^- and precipitation of the metal sulphide. ZnS nanoflowers, multipodal CdS nanostructures, and $Fe_{(1-x)}S$ platelets have been obtained by this method, with the particle shape determined by the underlying crystal structures of the products. By first passing the thiourea through the preheater prior to contact with the metal salt stream the

generation of HS^- and metal sulphide formation are separated. This results in a nucleation driven process, yielding nanoparticles of ZnS, CdS and PbS, with sizes determined by the chosen reaction temperature. Hexagonal nanoplatelets of CuS and $Fe_{(1-x)}S$, and Bi_2S_3 nanorod assemblies have also been obtained.

As the first reported use of continuous hydrothermal methods for the production of sulphide nanomaterials this work represents a significant advancement in the scope of continuous hydrothermal synthesis technology. In addition, the hydrothermal approach eliminates the need for the high boiling point solvents that are often used in the synthesis of metal sulphide nanomaterials by more conventional routes. This approach is thus significantly more environmentally friendly, and as a continuous process it is inherently scalable, making it suitable for large-scale industrial production of these materials.

Acknowledgements

This work is funded under the auspices of the European Union's Seventh Framework Programme (FP7/2007-2013), grant agreement no. FP7-NMP4-LA-2012-280983 SHYMAN. The authors wish to thank Dr. Mike Fay of the Nottingham Nanoscience and Nanotechnology Centre for access to and support with the HRTEM facilities. Dr. Nigel Neate and the Advanced Materials Research group in the Department of Mechanical, Materials and Manufacturing Engineering are gratefully acknowledged for the use of their X-ray diffraction facilities. Fluorescence measurements were obtained with thanks to Dr. Steve Briddon and the School of Biomedical Sciences, Nottingham.

Notes and References

Department of Chemical and Environmental Engineering, University of Nottingham, University Park, Nottingham, NG7 2RD, UK.

Electronic Supplementary Information (ESI) available: Experimental details, refinement procedure, fluorescence spectra of ZnS samples. See DOI: 10.1039/b000000x/

E-mail: Edward.Lester@nottingham.ac.uk; Tel: +44 (0)1159 514974

1. J. M. Costa-Fernández, R. Pereiro and A. Sanz-Medel, *TrAC, Trends Anal. Chem.*, 2006, **25**, 207-218.
2. P. F. Smet, I. Moreels, Z. Hens and D. Poelman, *Materials*, 2010, **3**, 2834-2883.
3. J. Wang, *Analyst*, 2005, **130**, 421-426.
4. P. Wu and X.-P. Yan, *Chem. Soc. Rev.*, 2013, **42**, 5489-5521.
5. Z. Tan, F. Zhang, T. Zhu, J. Xu, A. Y. Wang, J. D. Dixon, L. Li, Q. Zhang, S. E. Mohney and J. Ruzyllo, *Nano Lett.*, 2007, **7**, 3803-3807.
6. R. Plass, S. Pelet, J. Krueger, M. Grätzel and U. Bach, *J. Phys. Chem. B*, 2002, **106**, 7578-7580.
7. F. Di Benedetto, M. Borgheresi, A. Caneschi, G. Chastanet, C. Cipriani, D. Gatteschi, G. Pratesi, M. Romanelli and R. Sessoli, *Eur. J. Mineral.*, **18**, 283-287.
8. A. L. Routzahn, S. L. White, L.-K. Fong and P. K. Jain, *Isr. J. Chem.*, 2012, **52**, 983-991.
9. Y. Zhao and C. Burda, *Energy Environ. Sci.*, 2012, **5**, 5564-5576.
10. D. Rickard and G. W. Luther, *Chem. Rev.*, 2007, **107**, 514-562.
11. D. Faivre and D. Schüler, *Chem. Rev.*, 2008, **108**, 4875-4898.
12. E.-J. Kim, J.-H. Kim, A.-M. Azad and Y.-S. Chang, *ACS Appl. Mater. Interfaces*, 2011, **3**, 1457-1462.
13. B. Wu, H. Song, J. Zhou and X. Chen, *Chem. Commun.*, 2011, **47**, 8653-8655.
14. L.-D. Zhao, B.-P. Zhang, W.-S. Liu, H.-L. Zhang and J.-F. Li, *J. Solid State Chem.*, 2008, **181**, 3278-3282.
15. J. Joo, H. B. Na, T. Yu, J. H. Yu, Y. W. Kim, F. Wu, J. Z. Zhang and T. Hyeon, *J. Am. Chem. Soc.*, 2003, **125**, 11100-11105.
16. L.-J. Zhang, X.-C. Shen, H. Liang, S. Guo and Z.-H. Liang, *J. Colloid Interface Sci.*, 2010, **342**, 236-242.
17. T. Mandal, G. Piburn, V. Stavila, I. Rusakova, T. Ould-Ely, A. C. Colson and K. H. Whitmire, *Chem. Mater.*, 2011, **23**, 4158-4169.
18. S. Shen, Y. Zhang, L. Peng, B. Xu, Y. Du, M. Deng, H. Xu and Q. Wang, *Crystengcomm*, 2011, **13**, 4572-4579.
19. Z. Cheng, S. Wang, D. Si and B. Geng, *J. Alloys Compd.*, 2010, **492**, L44-L49.
20. Y. Ni, X. Wei, J. Hong and X. Ma, *Mater. Res. Bull.*, 2007, **42**, 17-26.
21. M. Salavati-Niasari, D. Ghanbari and F. Davar, *J. Alloys Compd.*, 2009, **488**, 442-447.
22. L. Wang, L. Chen, T. Luo and Y. Qian, *Mater. Lett.*, 2006, **60**, 3627-3630.
23. Q. Xia, X. Chen, K. Zhao and J. Liu, *Mater. Chem. Phys.*, 2008, **111**, 98-105.
24. A. M. Nightingale and J. C. de Mello, *J. Mater. Chem.*, 2010, **20**, 8454-8463.
25. E. M. Chan, R. A. Mathies and A. P. Alivisatos, *Nano Lett.*, 2003, **3**, 199-201.
26. D. R. Modeshia and R. I. Walton, *Chem. Soc. Rev.*, 2010, **39**, 4303-4325.
27. R. I. Walton, *Prog. Cryst. Growth Charact. Mater.*, 2011, **57**, 93-108.
28. K. Byrappa and T. Adschiri, *Prog. Cryst. Growth Charact. Mater.*, 2007, **53**, 117-166.
29. M. Yoshimura and K. Byrappa, *J. Mater. Sci.*, 2008, **43**, 2085-2103.
30. T. Adschiri, K. Kanazawa and K. Arai, *J. Am. Ceram. Soc.*, 1992, **75**, 1019-1022.
31. T. Adschiri, *Chem. Lett.*, 2007, **36**, 1188-1193.
32. T. Adschiri, Y. Hakuta and K. Arai, *Ind. Eng. Chem. Res.*, 2000, **39**, 4901-4907.
33. V. I. Anikeev, *Russ. J. Phys. Chem. A*, 2011, **85**, 377-382.
34. A. Cabanas, J. A. Darr, E. Lester and M. Poliakoff, *J. Mater. Chem.*, 2001, **11**, 561-568.
35. Y. Hakuta, H. Ura, H. Hayashi and K. Arai, *Ind. Eng. Chem. Res.*, 2005, **44**, 840-846.
36. E. Lester, G. Aksomaityte, J. Li, S. Gomez, J. Gonzalez-Gonzalez and M. Poliakoff, *Prog. Cryst. Growth Charact. Mater.*, 2012, **58**, 3-13.
37. T. Adschiri, Y. Hakuta, K. Sue and K. Arai, *J. Nanopart. Res.*, 2001, **3**, 227-235.
38. P. J. Blood, J. P. Denyer, B. J. Azzopardi, M. Poliakoff and E. Lester, *Chem. Eng. Sci.*, 2004, **59**, 2853-2861.
39. E. Lester, P. Blood, J. Denyer, D. Giddings, B. Azzopardi and M. Poliakoff, *J. Supercrit. Fluids*, 2006, **37**, 209-214.
40. E. Lester, P. J. Blood, J. P. Denyer, B. J. Azzopardi, J. Li and M. Poliakoff, *Mater. Res. Innovations*, 2010, **14**, 19-26.

41. T. Lin, S. Kellici, K. Gong, K. Thompson, J. R. G. Evans, X. Wang and J. A. Darr, *J. Comb. Chem.*, 2010, **12**, 383-392.
42. L. L. Toft, D. F. Aarup, M. Bremholm, P. Hald and B. B. Iversen, *J. Solid State Chem.*, 2009, **182**, 491-495.
43. Y. Wakashima, A. Suzuki, S.-i. Kawasaki, K. Matsui and Y. Hakuta, *J. Chem. Eng. Jpn.*, 2007, **40**, 622-629.
44. S.-A. Hong, S. J. Kim, J. Kim, K. Y. Chung, B.-W. Cho and J. W. Kang, *J. Supercrit. Fluids*, 2011, **55**, 1027-1037.
45. C. Xu, J. Lee and A. S. Teja, *J. Supercrit. Fluids*, 2008, **44**, 92-97.
46. A. A. Chaudhry, S. Haque, S. Kellici, P. Boldrin, I. Rehman, F. A. Khalid and J. A. Darr, *Chem. Commun.*, 2006, 2286-2288.
47. E. Lester, S. V. Y. Tang, A. Khlobystov, V. L. Rose, L. Buttery and C. J. Roberts, *Crystengcomm*, 2013, **15**, 3256-3260.
48. H. Choi, B. Veriansyah, J. Kim, J.-D. Kim and J. W. Kang, *J. Supercrit. Fluids*, 2010, **52**, 285-291.
49. G. Aksomaityte, M. Poliakoff and E. Lester, *Chem. Eng. Sci.*, 2013, **85**, 2-10.
50. M. Gimeno-Fabra, A. S. Munn, L. A. Stevens, T. C. Drage, D. M. Grant, R. J. Kashtiban, J. Sloan, E. Lester and R. I. Walton, *Chem. Commun.*, 2012, **48**, 10642-10644.
51. WO 2005077505 A2, 2005.
52. R. W. Cheary and A. A. Coehlo, CCP14 Powder Diffraction Library, Engineering and Physical Sciences Research Council, Daresbury Laboratory, Warrington, England, 1996.
53. A. C. Larson and R. B. Von Dreele, Los Alamos National Laboratory Report LAUR 86-748, 1994.
54. B. H. Toby, *J. Appl. Crystallogr.*, 2001, 210-213.
55. H. Zhang and J. F. Banfield, *J. Phys. Chem. C*, 2009, **113**, 9681-9687.
56. H. Zhang, B. Chen, B. Gilbert and J. F. Banfield, *J. Mater. Chem.*, 2006, **16**, 249-254.
57. H. Zhang, B. Gilbert, F. Huang and J. F. Banfield, *Nature*, 2003, **424**, 1025-1029.
58. Y. Cao, X. Hu, D. Wang, Y. Sun, P. Sun, J. Zheng, J. Ma and G. Lu, *Mater. Lett.*, 2012, **69**, 45-47.
59. Y. Guo, J. Wang, L. Yang, J. Zhang, K. Jiang, W. Li, L. Wang and L. Jiang, *Crystengcomm*, 2011, **13**, 5045-5048.
60. Z. Huijuan and Q. Limin, *Nanotechnology*, 2006, **17**, 3984.
61. M. A. Mahdi, J. J. Hassan, Z. Hassan and S. S. Ng, *J. Alloys Compd.*, 2012, **541**, 227-233.
62. Y. Shi, J. Chen and P. Shen, *J. Alloys Compd.*, 2007, **441**, 337-343.
63. G. W. Luther III, S. M. Theberge and D. T. Rickard, *Geochim. Cosmochim. Acta*, 1999, **63**, 3159-3169.
64. M. Chen, Y. Xie, J. Lu, Y. Xiong, S. Zhang, Y. Qian and X. Liu, *J. Mater. Chem.*, 2002, **12**, 748-753.
65. L. Manna, E. C. Scher and A. P. Alivisatos, *J. Am. Chem. Soc.*, 2000, **122**, 12700-12706.
66. D. V. Talapin, J. H. Nelson, E. V. Shevchenko, S. Aloni, B. Sadtler and A. P. Alivisatos, *Nano Lett.*, 2007, **7**, 2951-2959.
67. Z. Fan, A. O. Yalcin, F. D. Tichelaar, H. W. Zandbergen, E. Talgorn, A. J. Houtepen, T. J. H. Vlugt and M. A. van Huis, *J. Am. Chem. Soc.*, 2013, **135**, 5869-5876.
68. S. Kudera, L. Carbone, E. Carlino, R. Cingolani, P. D. Cozzoli and L. Manna, *Phys. E*, 2007, **37**, 128-133.
69. F. Huang and J. F. Banfield, *J. Am. Chem. Soc.*, 2005, **127**, 4523-4529.
70. E. Koupanou, S. Ahualli, O. Glatter, A. Delgado, F. Krumeich and E. Leontidis, *Langmuir*, 2010, **26**, 16909-16920.
71. Y. C. Zhang, T. Qiao, X. Y. Hu, G. Y. Wang and X. Wu, *J. Cryst. Growth*, 2005, **277**, 518-523.
72. Y. Ni, F. Wang, H. Liu, G. Yin, J. Hong, X. Ma and Z. Xu, *J. Cryst. Growth*, 2004, **262**, 399-402.
73. A. Querejeta-Fernández, J. C. Hernández-Garrido, H. Yang, Y. Zhou, A. Varela, M. Parras, J. J. Calvino-Gámez, J. M. González-Calbet, P. F. Green and N. A. Kotov, *ACS Nano*, 2012, **6**, 3800-3812.
74. W. H. R. Shaw and D. G. Walker, *J. Am. Chem. Soc.*, 1956, **78**, 5769-5772.
75. E. J. Newman, *Analyst*, 1963, **88**, 500-505.
76. P. Kumar, R. Nagarajan and R. Sarangi, *J. Mater. Chem. C*, 2013, **1**, 2448-2454.
77. H. T. Evans Jr. and J. A. Konnert, *Am. Mineral.*, 1976, **61**, 996-1000.
78. F. Li, T. Kong, W. Bi, D. Li, Z. Li and X. Huang, *Appl. Surf. Sci.*, 2009, **255**, 6285-6289.
79. Z. Cheng, S. Wang, Q. Wang and B. Geng, *Crystengcomm*, 2010, **12**, 144-149.
80. K. Tang, D. Chen, Y. Liu, G. Shen, H. zheng and Y. Qian, *J. Cryst. Growth*, 2004, **263**, 232-236.
81. J. D. Miller, J. Li, J. C. Davidtz and F. Vos, *Miner. Eng.*, 2005, **18**, 855-865.
82. H.-Y. Lai and C.-J. Chen, *J. Cryst. Growth*, 2009, **311**, 4698-4703.
83. A. Phuruangrat, T. Thongtem and S. Thongtem, *Mater. Lett.*, 2009, **63**, 1496-1498.
84. J. Lu, Q. Han, X. Yang, L. Lu and X. Wang, *Mater. Lett.*, 2007, **61**, 2883-2886.
85. Q. Wang, X. Wang, W. Lou and J. Hao, *New J. Chem.*, 2010, **34**, 1930-1935.
86. S. Kumar and T. Nann, *Small*, 2006, **2**, 316-329.
87. V. K. LaMer and R. H. Dinegar, *J. Am. Chem. Soc.*, 1950, **72**, 4847-4854.